PHYSICAL REVIEW FLUIDS **00**, 004900 (2025)

Filiform microswimmers in tubular confinements

Adnan Morshed,* Ricardo Cortez,† and Lisa Fauci‡
Department of Mathematics, Tulane University, New Orleans, Louisiana 70118, USA

(Received 4 July 2025; accepted 23 September 2025; published xxxxxxxxxx)

Storage of sperm in the female reproductive tract occurs across species that reproduce by internal fertilization, modulating availability and preserving fertility. For instance, the sperm of the insects from the family *Drosophilidae* are stored in and released from the seminal receptacle—a long, slender, coiled tube. The sperm flagella, longer than any straight portion of the tube, must be flexible enough to navigate the twists and turns of these tightly coiled organs. As a step towards studying the coupled system of fluid, tube geometry, and flexible flagella, we present here a framework to study flagellar motion in tubular enclosures. The basic swimmer is modeled as a flexible Kirchhoff rod comprised of regularized Stokeslet segments, while the rigid surfaces that constitute the enclosure are represented by regularized Stokeslet surfaces. Swimming kinematics is not prescribed, but emerges from time-varying preferred curvatures. This approach allows for swimmer-wall interactions and, in turn, the evolution of swimming behavior near rigid boundaries. We first investigate the effects of flagellar bending rigidity, beat frequency, and the presence of inactive flagellar regions on swimming performance in free space. Next, we study the effect of confinement levels on swimming performance inside straight tubes. We find that swimming speed increases as the tube diameter decreases, with a more pronounced boost in speed for stiffer flagella. We also find that the swimmers, whose preferred beat is planar, drift towards the tube walls if the diameter of the tube is large enough. Finally, our work demonstrates that the model flagellum can navigate through a curved tube, which will enable studies aimed at understanding the coevolution of female reproductive tracts and sperm morphology in different organisms.

DOI: 10.1103/7t6v-w8sv

I. INTRODUCTION

A classical problem in biological fluid dynamics at the microscale is the motility of a flagellum undergoing sinusoidal oscillations in an unbounded Newtonian fluid. Beginning with Taylor's analysis of the progression of swimming sheets or cylinders in the 1950s [1,2], the study of the fluid dynamics of micro-organisms, both natural and engineered, has enjoyed much success in the last decades, through advances in imaging technologies, computational methods, microfluidic devices, material science, and non-Newtonian fluid dynamics (e.g., [3–8]). Many, if not most, of the biological examples of microscale propulsion rarely happen in spaces that can be satisfactorily considered "free-space swimming" in the mathematical sense. Rather, both the swimmers and background flows are strongly influenced by the surrounding confines established by vessel walls [9], membranes [10], porous matrices [11], or other fluid-solid [12–15] and fluid-fluid interfaces [16,17]. Early experimental observations of the effect of boundaries on sperm [18] report that they do

*Contact author: amorshed@tulane.edu
†Contact author: rcortez@tulane.edu
‡Contact author: fauci@tulane.edu

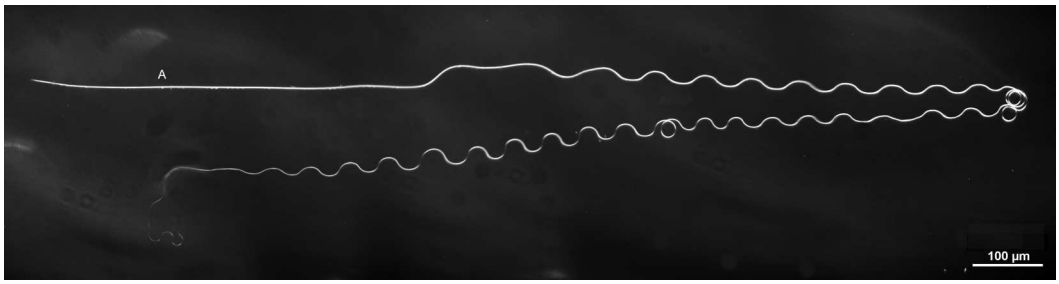

FIG. 1. *Drosophila montana* sperm; A identifies the head area. The sperm cell is 3.48 mm long. Image was taken with a 20× objective, courtesy of Hadlow and Snook, Stockholm University.

accumulate near a surface, and these findings were further detailed in [19]. Mammalian sperm navigation through the female reproductive tract has been studied experimentally, showing the presence of both chemotactic and boundary-induced hydrodynamic effects [20,21]. More recent microfluidic experiments with sperm cells have also explored rheotactic behavior and steering effects induced by rigid boundaries [13,22].

An intriguing example of long flagella moving through narrow confinements is that of the sperm of the fruit fly making its journey through the female fly's reproductive tract [23]. While human sperm flagella are about 50 microns long, the *Drosophila montana* shown in Fig. 1 is over three millimeters long, which is on the order of the fly's actual body length. Clearly, in order for this sperm flagellum to traverse the coiled female reproductive tract, it must be flexible enough to bend. Here we will present a model of this coupled elastohydrodynamic system using a computational framework that captures the dynamics of the flexible flagellum, its emergent waveform, and the geometry of the tubular confinement.

Hydrodynamic models of flagellar motility may be classified according to a hierarchy of specifications of shape dynamics. In the simplest class of models, the flagellar *kinematics are prescribed*, and do not deviate from this prescription no matter what forces are felt from the viscous load, neighboring organisms, or nearby boundaries [24–27]. In the Stokes regime, the total force and torque exerted by the free swimmer must be zero. These constraints are satisfied by allowing a rigid translation and rotation of the swimmer. These models may be used to analyze the fluid flow generated by the given motion and the forces required to achieve the prescribed shape.

In the second class of models, the flagellum is in pursuit of a *preferred shape*, and exerts forces on the fluid that are derived from tensile and bending energies. Stiffness constants related to the bending rigidity of the flagellum determine the extent to which the preferred shape is achieved (e.g., [28–31]). In these models, the choice of the target shape may come from experimental observations or may evolve from other features of the model, such as biochemical signaling [32]. Finally, the third class of flagellar models is one in which kinematics are not prescribed, nor a preferred shape input, but one where the kinematics emerge from the fully coupled system of fluid environment, passive elastic properties, and the action of the internal dynein motors on the axonemal structure. Flagellar models of this last class are found in [3,29,33–35]. The model discussed here will be from the second class, a preferred-curvature model, which does capture the flexibility of the flagellum and its shape deformations from interaction with the viscous fluid and boundaries.

The effect of boundaries on micro-organism swimming has been the subject of numerous computational models, using immersed boundary methods, boundary element methods, and reduced order representations of swimmers [19,36–41]. Within the context of computational models based upon fundamental solutions of the Stokes equations, such as boundary integral methods or the method of regularized Stokeslets, a standard approach to model swimmer-surface interactions is to use the method of images to enforce the zero-velocity condition on a planar rigid wall [42,43]. However, the image-based approach is not suitable for more complex geometries like tubular

vessels, where fundamental solutions are not analytically available. As in [44], which used a regularized Stokeslet model of swimming flexible helices within a cylinder, we will explicitly represent the tubular confinement and enforce the no-slip condition. In this paper, we describe our mathematical modeling efforts in developing a robust, dynamical model of a filiform flagellum swimming within a confinement. The flagellum embodies characteristics like flexibility, active, and passive sections along its length, and modulation of shape amplitude and frequency. The model builds on the regularized Stokeslet segment [45] formulation in which the flagellum is taken to be a Kirchhoff elastic rod with collections of piecewise linear distributions of forces and torques on rod segments. Forces and torques along the rod arise from *preferred intrinsic curvatures and twists* that are prescribed along its centerline. This regularized Stokeslet segment approach allows the resolution of a given sinusoidal wave using many fewer discretization points than the standard regularized Stokeslet [46] formulation, and hence will allow efficient modeling of very long flagella. In addition, we present an extension of the regularized Stokeslet method to form solid, no-slip boundaries [47] that is used to construct both straight and tortuous fluid-filled enclosures. In the following sections, we first discuss the methodology used to model the flagellar-tubular system. Then, for a flagellum in free space, we analyze the effects of inhomogeneous activation, variation of beat frequency, variation of bending rigidity, and flagellar length on hydrodynamic performance. We then investigate the full elastohydrodynamic coupled system of a flexible flagellum moving through a straight tube. Finally, we demonstrate that in the case of a curved tube where the flagellum is considerably longer than any straight portion of the tube, the flagellum cannot meet its preferred shape, but must curve to traverse the tube. We remark that hydrodynamic flagellar models of the first class, which prescribe flagellar kinematics, cannot be used in such confined geometries.

II. METHODOLOGY

This section describes the components of the model of a self-propelled flagellum in a tubular space. The model consists of several elements that affect the dynamics of the flagellum, including the forces that develop along the length of the flagellum to generate the beat, the fluid motion generated by the flagellar forces, the forces along the tube surface, and the fluid motion they produce. It will also be necessary to include a strategy to prevent the flagellum and surface from occupying the same volume during the numerical updates of the flagellar shape.

A. Actuation of swimming filament

We describe the sperm flagellum as an active filament immersed in a viscous, incompressible fluid whose motion is described by the Stokes equations. The active filament, with the assumption that its length is much larger compared to its radius, is modeled as a one-dimensional slender rod with the freedom to bend and twist. Following [48], we use a modified Kirchhoff rod framework to approximate the dynamical behavior of the filament as an elastic rod.

The Kirchhoff framework represents the rod's centerline as a space curve $\mathbf{X}(s,t)$ and a set of local orthonormal reference frames, $\{\mathbf{D}^1(s,t), \mathbf{D}^2(s,t), \mathbf{D}^3(s,t)\}$ at each point on the curve (Fig. 2). We set the Lagrangian parameter s as the arclength of the rod of length L and assume a constant cross-sectional radius along the arclength. The orthonormality of the triads in each set of director basis is maintained by the constraint $\mathbf{D}^i \cdot \mathbf{D}^j = \delta_{ij}; i, j = 1, 2, 3$. By convention, $\mathbf{D}^3$ coincides with the unit vector tangent to the curve.

For any section of the rod, internal forces $\mathbf{F}$ and internal couples $\mathbf{N}$ are transmitted through the cross-sections by averaging the stresses acting across them. These internal forces and couples are computed from the current geometry of the flagellum. The constitutive relations for internal forces are

$$F^1 = b_1 \mathbf{D}^1 \cdot \frac{\partial \mathbf{X}}{\partial s}, \quad F^2 = b_2 \mathbf{D}^2 \cdot \frac{\partial \mathbf{X}}{\partial s}, \quad F^3 = b_3 \left(\mathbf{D}^3 \cdot \frac{\partial \mathbf{X}}{\partial s} - 1 \right), \tag{1}$$

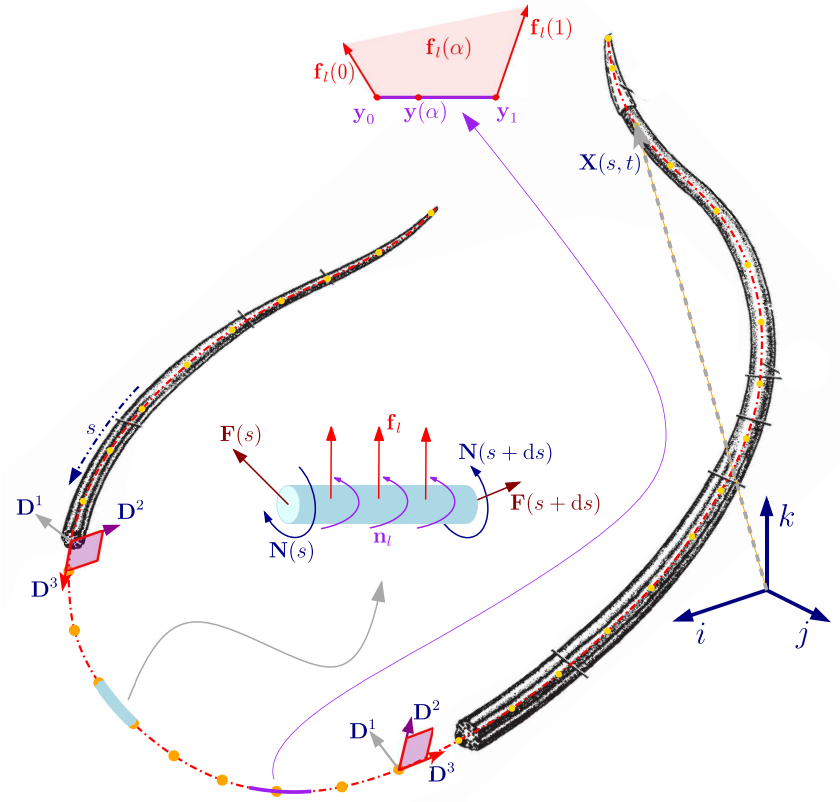

FIG. 2. Lagrangian variables for a typical representation of a swimming micro-organism in the Kirchhoff rod framework. Distance between points on the organism is tracked with the arclength parameter s, while orthogonal directors $\{\mathbf{D}^1, \mathbf{D}^2, \mathbf{D}^3\}$ at each of the Lagrangian points are used to track bend and rotation. We also highlight the linearly varying nature of force (and torque) densities of the regularized Stokeslet segment framework and the balance of internal and surface forces (and moments) for a standard Kirchhoff rod. Background image reproduced from [49].

where b_1 and b_2 are the shear moduli, and b_3 is the extension modulus. Values of these moduli are chosen to be large enough so that the filament approximately satisfies the unshearability and inextensibility conditions. Moreover, the penalty formulation for F^3 in Eq. (1) also tends to maintain $\mathbf{D}^3$ tangent to the centerline of the rod. All Lagrangian variables are expanded in terms of the local coordinates.

The constitutive equations for the internal moments are

$$N^1 = a_1\left(\frac{\partial \mathbf{D}^2}{\partial s}\cdot\mathbf{D}^3 - \Omega_1\right), \quad N^2 = a_2\left(\frac{\partial \mathbf{D}^3}{\partial s}\cdot\mathbf{D}^1 - \Omega_2\right), \quad N^3 = a_3\left(\frac{\partial \mathbf{D}^1}{\partial s}\cdot\mathbf{D}^2 - \Omega_3\right). \tag{2}$$

Here, a_1 and a_2 are the bending moduli (equal in the case of an isotropic and homogeneous rod with circular cross-section and constant radius along the arclength), a_3 is the twisting modulus, and $\mathbf{\Omega}(s,t) = \{\Omega_1, \Omega_2, \Omega_3\}$ is the driving (preferred) strain bend-twist vector. We refer to its components as the preferred target curvatures, and they are derived from an idealized time-varying planar sinusoidal preferred shape for the flagellum. As in [50], a general time-varying preferred shape $\mathbf{X}(s,t) = x_1(s,t)\hat{i} + x_2(s,t)\hat{j} + x_3(s,t)\hat{k}$ parametrized by the arclength can be expressed in terms of the preferred bend-twist vector $\{\Omega_1(s,t), \Omega_2(s,t), \Omega_3(s,t)\}$ (see below).

This leads to the following force and couple balances:

$$\mathbf{f}_l + \frac{\partial \mathbf{F}}{\partial s} = 0, \tag{3}$$

$$\mathbf{n}_l + \frac{\partial \mathbf{N}}{\partial s} + \left(\frac{\partial \mathbf{X}}{\partial s} \times \mathbf{F}\right) = 0, \tag{4}$$

where $\mathbf{f}_l$ and $\mathbf{n}_l$ are force density per unit length (in s) and torque density per unit length (in s) applied to the rod segment by the surrounding fluid.

The simulations in this work use the preferred shape

$$x_1(s,t) = A\cos(ks - \omega t) \text{ and } x_2(s,t) = 0,$$

where A, k, and ω are the preferred amplitude, wave number, and angular frequency, respectively. The third component, $x_3(s,t)$, is computed by solving the ordinary differential equation resulting from the tangent vector constraint $(x_1'^2 + x_2'^2 + x_3'^2)^{1/2} = 1$. As such, the preferred bend-twist vectors become

$$\Omega_1(s,t) = x_1' x_3'' - x_3' x_1'' = \frac{x_1''}{\sqrt{1 - x_1'^2}}, \quad \Omega_2(s,t) = 0, \quad \Omega_3(s,t) = 0,$$

where we used $x_3' = \sqrt{1 - x_1'^2}$ and $x_3'' = -x_1' x_1''/\sqrt{1 - x_1'^2}$. The calculated strain twist vector represents the time-dependent preferred curvature $[(s,t) = \sqrt{\Omega_1^2 + \Omega_2^2}]$ and twist Ω_3 of the rod centerline.

The balance of force and couple is accomplished by introducing a force per unit length $\mathbf{f}_l$ and a torque per unit length $\mathbf{n}_l$ exerted by the fluid on the flagellum, which result in a flagellum shape that approximates the curvatures of the preferred bend-twist vector. The curvature and twist that are actually achieved by the flagellum depend on several factors, including fluid-structure interactions, structure-structure interactions, as well as mechanical properties of the structure. At any given time t, at a point s on the flagellum, the achieved bend twist vector component $\Omega_{i,\mathrm{ach}}(s,t)$ is expressed in terms of the local directors as

$$\Omega_{i,\mathrm{ach}}(s,t) = \frac{\partial \mathbf{D}^j(s,t)}{\partial s} \cdot \mathbf{D}^k(s,t), \tag{5}$$

where (i, j, k) is any cyclic permutation of $(1, 2, 3)$. The differences $[\Omega_{i,\mathrm{ach}}(s,t)$ versus $\Omega_i(s,t)]$ appear in the constitutive equations for torques [Eq. (2)] and produce the internal moment densities driving the motion.

In summary, the actuation of the filament is accomplished by computing force and torque densities along the flagellum based on the difference between the configuration of the flagellum and the time-dependent preferred bend-twist vector, $\mathbf{f}_l(s,t)$ and $\mathbf{n}_l(s,t)$, along the flagellum length. While these force and torque densities produce self-propulsion, the net force and net torque on the flagellum are zero. Next, we describe how these forces and torques generate fluid motion.

B. Regularized Stokeslet segments and regularized Stokeslet surfaces

In this section, we provide expressions for the fluid motion due to force per unit length $\mathbf{f}_l(s,t)$ and a torque per unit length $\mathbf{n}_l(s,t)$ along the Kirchhoff rod. The motion of a viscous, incompressible flow in three dimensions at zero Reynolds number is modeled with the Stokes equations:

$$\mu\nabla^2\mathbf{u} = \nabla p - \mathbf{f}_b - \tfrac{1}{2}\nabla \times \mathbf{n}_b, \tag{6}$$

$$\nabla \cdot \mathbf{u} = \mathbf{0}, \tag{7}$$

$$\mathbf{f}_b = \int_0^L \mathbf{f}_l(s,t)\delta(\hat{x} - \mathbf{X}(s,t))\,\mathrm{d}s, \tag{8}$$

$$\frac{1}{2}\nabla \times \mathbf{n}_b = \int_0^L \frac{1}{2}\nabla \times \mathbf{n}_l(s,t)\delta(\hat{x} - \mathbf{X}(s,t))\,\mathrm{d}s, \tag{9}$$

2

where μ is the dynamic viscosity, $\mathbf{u}$ is the fluid velocity, p is the pressure, and $\mathbf{f}_b$ and $\mathbf{n}_b$ are the force and torque per unit volume on the fluid. The velocity expression that we develop here is based on the fluid velocity at an arbitrary point $\hat{x}$ in the domain due to a single point force concentrated at the location $\mathbf{y}$. For the derivation, we assume temporarily that there is only one point force $\mathbf{F}_b$ with associated force density $\mathbf{f}_b = \mathbf{F}_b\delta(\hat{x} - \mathbf{y})$, where δ is the three-dimensional Dirac delta function. The velocity due to this force is the Stokeslet [51,52]:

$$\mathbf{u}(\hat{x}) = \frac{1}{8\pi\mu}\left[\frac{\mathbf{F}_b}{r} + \frac{(\mathbf{r}\cdot\mathbf{F}_b)\mathbf{r}}{r^3}\right], \tag{10}$$

where $\mathbf{r}(\hat{x}) = \hat{x} - \mathbf{y}$, and $r = |\mathbf{r}|$.The Stokeslet expression has a singularity of the form r^{-1}, which can present difficulties when the forces are distributed on curves or at scattered points in three dimensions. One approach to modeling the forces along the flagellum without producing singularities in the fluid domain is to mollify the forces so that they are not concentrated in an infinitesimally thin curve, but are spread over a small surrounding region [53]. This approach replaces the Dirac delta function in the expression of the force per volume with $\mathbf{f}_b = \mathbf{F}_b\phi_\epsilon(\hat{x} - \mathbf{y})$, where ϕ_ϵ is a radially symmetric regularizing function (blob) which satisfies $\iiint \phi_\epsilon(\mathbf{r})\,\mathrm{d}\mathbf{r} = 1$. There are many functions, including Gaussian, exponential, and algebraic, that can be used. A common choice is

$$\phi_\epsilon(\mathbf{r}) = \frac{15\epsilon^4}{8\pi(r^2+\epsilon^2)^{7/2}},$$

where ϵ is a small regularization parameter that controls the size of the extent of the force. This leads to an exact solution of the Stokes equations called the regularized Stokeslet,

$$\mathbf{u}(\hat{x}) = \frac{1}{8\pi\mu}\left[\left(\frac{1}{R_\epsilon} + \frac{\epsilon^2}{R_\epsilon^3}\right)\mathbf{F}_b + \frac{(\mathbf{F}_b\cdot\mathbf{r})\mathbf{r}}{R_\epsilon^3}\right], \tag{11}$$

TABLE I. Reference parameters and scales for the swimmer model used throughout this study. The twist modulus is assumed to have the same magnitude as the bending moduli, while the shear and stretch moduli are chosen to be large enough to maintain unshearability and inextensibility. We choose water as the fluid medium in our simulations.

Parameter	Interpretation	Representative value	References
L	Flagellar length	100 μm	[54,55]
$EI = a_1 = a_2$	Bending moduli	4.95×10^{-21} J m	[56–60]
a_3	Twist modulus	4.95×10^{-21} J m	
$b_1 = b_2 = b$	Shear moduli	8.3×10^{-10} kg m s^{-2}	
$b_3 = b$	Stretch modulus	8.3×10^{-10} kg m s^{-2}	
$f = \omega/2\pi$	Beat frequency	20 Hz	[61]
A	Preferred beat amplitude	2 μm	[61]
λ	Wavelength	33.33 mm	[61]
k	Wave number	$k = 2\pi/\lambda$	
μ	Fluid viscosity	0.001 kg m^{-1} s^{-1}	

where $R_\epsilon^2 = |\mathbf{r}|^2 + \epsilon^2$. Similarly, for a regularized point torque $\mathbf{n}_b = \mathbf{N}_b \phi_\epsilon(\hat{x} - \mathbf{y})$, the velocity is

$$\mathbf{u}(\hat{x}) = \frac{1}{8\pi\mu}\left(\frac{2}{R_\epsilon^3} + \frac{3\epsilon^2}{R_\epsilon^5}\right)(\mathbf{N}_b \times \mathbf{r}). \tag{12}$$

1. A Kirchhoff rod as a continuum of regularized Stokeslets

Returning to the case of the Kirchhoff rod described in Eq. (6), the velocity field produced by the flagellar forces and torques is given by an integral along the flagellum. We use the method of regularized Stokeslet segments [45], where the flagellum is represented by a piecewise linear curve with a linear continuous distribution of regularized forces along each line segment:

$$\mathbf{u}_F(\hat{x}) = \frac{\ell}{8\pi\mu}\int_0^1 \left[\left(\frac{1}{R_\epsilon} + \frac{\epsilon^2}{R_\epsilon^3}\right)\mathbf{f}_l(\alpha) + \frac{[\mathbf{f}_l(\alpha)\cdot\mathbf{r}(\alpha)]\mathbf{r}(\alpha)}{R_\epsilon^3}\right] \mathrm{d}\alpha, \tag{13}$$

where $\mathbf{r}(\alpha) = \hat{x} - \mathbf{y}(\alpha)$ is now dependent on the location along the segment as well ($0 \leqslant \alpha \leqslant 1$). Here, $\mathbf{y}(\alpha) = \mathbf{y}_0 + \alpha(\mathbf{y}_1 - \mathbf{y}_0)$, and $\mathbf{f}_l(\alpha) = \mathbf{f}_{l,0} + \alpha(\mathbf{f}_{l,1} - \mathbf{f}_{l,0})$. Similarly, for a linearly varying continuous distribution of torque density (per unit length) $\mathbf{n}_l(\alpha)$ on a line segment, the velocity is evaluated through

$$\mathbf{u}_T(\hat{x}) = \frac{\ell}{8\pi\mu}\int_0^1 \left[\left(\frac{2}{R_\epsilon^3} + \frac{3\epsilon^2}{R_\epsilon^5}\right)[\mathbf{n}_l(\alpha)\times\mathbf{r}(\alpha)]\right] \mathrm{d}\alpha, \tag{14}$$

where $\mathbf{n}_l(\alpha) = \mathbf{n}_{l,0} + \alpha(\mathbf{n}_{l,1} - \mathbf{n}_{l,0})$. Analytical expressions for these integrals, derived in [45], are used to evaluate the fluid velocity at an arbitrary evaluation point $\hat{x}$ due to flagellar forces. Since the forces are a continuous function on the flagellum, the two numerical parameters involved—the length ℓ of a segment and the regularization parameter ϵ—are essentially decoupled and can be selected based on physical arguments.

2. Regularized Stokeslet surfaces

The idea of continuously varying forces and torques along a line segment is extended in Ref. [47], where the fluid motion is generated by forces distributed over surfaces. Here, a surface embedded in a three-dimensional flow is discretized with nodes forming the vertices of triangles. The surface is assumed to be planar in each triangle, where a linear force vector field is considered on each triangular patch of surface. This is similar to a finite-element method with linear elements over triangles. However, the velocity is computed by analytically integrating regularized Stokeslets due to the linear forces over a flat triangular surface patch. Effectively, this velocity is due to a continuum of linear force on the triangle (of area BH/2) and can be expressed as

$$\mathbf{u}_S(\hat{x}) = \frac{\mathrm{BH}}{8\pi\mu}\int_0^1\int_0^\alpha \left[\left(\frac{1}{R_\varsigma} + \frac{\varsigma^2}{R_\varsigma^3}\right)\mathbf{f}_a(\alpha,\beta) + \frac{[\mathbf{f}_a(\alpha,\beta)\cdot\mathbf{r}]\mathbf{r}}{R_\varsigma^3}\right] \mathrm{d}\beta\,\mathrm{d}\alpha, \tag{15}$$

where we assume a bilinear distribution of forces on the patch resulting on the force density (per unit area) $\mathbf{f}_a(\alpha,\beta) = \mathbf{f}_{a,0} + \alpha(\mathbf{f}_{a,1} - \mathbf{f}_{a,0}) + \beta(\mathbf{f}_{a,2} - \mathbf{f}_{a,1})$, based on the three vertex forces ($0 \leqslant \alpha \leqslant 1$ and $0 \leqslant \beta \leqslant \alpha$). As with the Stokeslet segments, here we define the distance $\mathbf{r} = \mathbf{r}(\alpha,\beta) = \hat{x} - \mathbf{y}(\alpha,\beta)$, and we introduce the surface regularization parameter ς in $R_\varsigma = \sqrt{|\mathbf{r}|^2 + \varsigma^2}$. The regularized forces overlap with neighboring forces regardless of the size of the parameter ς. In practice, this allows ς to be much smaller than if the force is a discrete set located only at the nodes. In [47], second-order convergence in the spatial discretization for fixed ς was demonstrated. A key advantage of this method is that it integrates a continuous, linear force exactly over triangular surface elements. Consequently, the regularization parameter can be reduced significantly while keeping the surface discretization fixed, without increasing the error [47]. This allows the use of minimal regularization, which results in very little thickening of the surface.

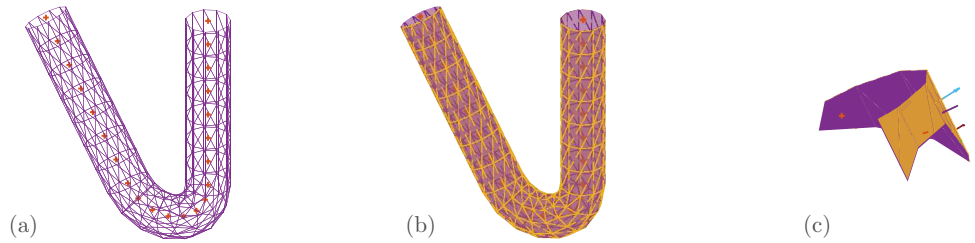

FIG. 3. The generation of the tubular confinement begins by (a) defining the centerline of the tube (red stars), and creating a cylindrical mesh around it; and (b) creating the sleeve as a second set of surface nodes slightly apart (the gap is 1% of the tube radius) from the cylindrical mesh. A zoomed-in view of the tube and the sleeve is shown in (c), where normal vectors are also shown. Note that the actual tube will have much higher point density.

Figure 3(a) shows the construction of a tubular structure with surface elements. We first define the centerline of the tubular section and subdivide it into equally spaced points. These points are used as centers to generate circles that form the physical surface of the tube wall. Adjacent surface points $\hat{x}_p$ are connected to create triangular patches that represent the surface of the tube. Since the tube wall is stationary and rigid, surface forces must develop to generate a fluid velocity on the tube nodes $\hat{x}_p$ that cancels the velocity generated by the flagellum at those points. We achieve this by solving the linear system for the force densities (force per area) in Eq. (15) for a given velocity on the left-hand side.

There is flexibility in choosing the location of these wall-force densities, which do not have to be the same set of nodes where the surface velocity boundary condition is enforced. We have found that if the location of a surface force comes arbitrarily close to a flagellum point, the force that develops can be very large, affecting the time step in the computation. However, this is not the case when there is a minimum separation between the surface force location and the flagellar force node. Therefore, a new set of points slightly offset outward from the tube surface points is created. We refer to these points as a sleeve and denote them as $\hat{x}_s$ [Figs. 3(b) and 3(c)].

Even with the no-slip condition enforced at the vertices of the triangular patches of the tube surface, the flagellum can pass through the tube surface for a fixed spatial and temporal discretization. Previous numerical studies have approached this issue by introducing a steric repulsion that only becomes active in the extreme vicinity of a solid wall [40,62,63]. The formulation of the force density follows the form of colloidal particle-particle electrostatic repulsion [64,65]. We use a slight variation to account for a finite repulsion at the wall, and we also introduce a cutoff beyond a threshold distance,

$$\mathbf{f}_{l,\mathrm{rep}} = \begin{cases} \mathcal{M}\xi \frac{\exp(-\rho/d)}{\xi + [1-\exp(-\rho/d)]}\hat{n} & \text{if } \rho \leqslant d, \\ 0 & \text{otherwise,} \end{cases} \tag{16}$$

where $\mathcal{M} = 20\ \mathrm{N\,m^{-1}}$ and $d =$ tube radius/40 are magnitude and distance parameters adjusted for our choice of simulation parameters, ρ is the distance from a point $\mathbf{y}(\alpha)$ on the flagellum to the nearest tube/wall patch, $\hat{n}$ is the unit normal vector pointing from the wall patch toward the flagellum, and ξ is a small nondimensional parameter to constrain the maximum repulsion force density. The repulsion force is added as a linear force density to $\mathbf{f}_l(\alpha)$ on the segments containing $\mathbf{y}(\alpha)$ whenever this flagellum point moves within the cutoff distance from the wall surface.

C. Algorithm summary

In summary, at any given time $t = t_n$, with a flagellum configuration given by $\mathbf{X}(s_j, t_n)$ and $\mathbf{D}^i(s_j, t_n)$, for $0 \leqslant j \leqslant M$, the numerical algorithm to advance the flagellum to the next time level t_{n+1} is described below. The velocity of each flagellum point has contributions from the flagellum

forces and torques, the tube sleeve, and any repulsion forces. The unit vectors $\mathbf{D}^i(s_j, t_n)$ rotate with the angular velocity generated by the velocity field.

(1) Update the preferred bend-twist vectors $\{\Omega_1(s_j, t_n), \Omega_2(s_j, t_n), \Omega_3(s_j, t_n)\}$ corresponding to the preferred flagellum shape at time t_{n+1}. Using the constitutive equations [Eqs. (1) and (2)], compute the internal force and moments from the Kirchhoff rod.

(2) Check if any portion of the flagellum is in the proximity of the tube surface for repulsion to be activated, and add the repulsion force density [Eq. (16)] to other forces already computed at those flagellum points.

(3) Use Eqs. (3) and (4) to evaluate forces and torques (per unit length) transmitted from the flagellum points to the fluid.

(4) Next use Eqs. (13) and (14) to compute the contribution to the flagellum velocities, $\mathbf{u}_F(\mathbf{X}(s_j, t_n))$ and $\mathbf{u}_T(\mathbf{X}(s_j, t_n))$, due to repulsion forces and the internal forces and moments.

(5) Use Eqs. (13) and (14) again, but this time to evaluate fluid velocities $\mathbf{u}(\hat{x}_p)$, at the tube/wall locations, $\hat{x}_p$. Solve the linear system in Eq. (15) to calculate force densities (per unit area) $\mathbf{f}_a(\hat{x}_s)$ at the sleeve patch vertices that produce the negative velocity field, $-\mathbf{u}(\hat{x}_p)$, at the tube/wall nodes.

(6) Use the surface forces just computed and Eq. (15) to compute the contribution to the flagellum velocity $\mathbf{u}_S(\mathbf{X}(s_j, t_n))$ due to surface forces that nullify any slip velocities on the tube surface.

(7) Add velocity contributions from steps 4 and 6 to compute the final velocity of the flagellum, $\mathbf{u}(\mathbf{X}(s_j, t_n))$ for $0 \leqslant j \leqslant M$. Update flagellum location as well as the director orientation using

$$\frac{\partial \mathbf{X}(s,t)}{\partial t} = \mathbf{u}(\mathbf{X}(s,t),t), \tag{17a}$$

$$\frac{\partial \mathbf{D}^i(s,t)}{\partial t} = \mathbf{w}(\mathbf{X}(s,t),t) \times \mathbf{D}^i(s,t), \quad i = 1,2,3, \tag{17b}$$

where $\mathbf{w}(\mathbf{X}(s,t)) = \frac{1}{2}\nabla \times \mathbf{u}(\mathbf{X}(s,t),t)$. Note that our implementation omits the contribution from surface forces to the velocity in the expression for $\mathbf{w}(\mathbf{X}(s,t),t)$. This approximation had little effect on the dynamics of the system.

Figure 4 illustrates the flagellar-tube system at two timepoints in a simulation: first when the flagellum is just entering the tubular structure [Figs. 4(a)–4(c)], and later when it is fully within the tube [Figs. 4(d)–4(f)]. The preferred waveform is planar, and the sinusoidal shape of the flagellum is evident in the "frontal" view in Fig. 4(a), with the corresponding "sagittal" view in Fig. 4(b) showing just a straight line. However, the flagellum in Fig. 4(e) no longer looks like a straight line, showing that the tube walls caused it to rotate out of its initial plane. Also depicted in Fig. 4 are velocity vectors at some chosen Eulerian positions within the tube, using the same locations at each of the two timepoints. The perspective views in Figs. 4(c) and 4(f) illustrate that the velocity on the tube walls is zero.

III. MODEL RESULTS

A. Free-space swimming

1. Comparison with Taylor's waving cylinders

We begin this section by presenting a comparison between the swimming speed of the planar flagellum from our model and that proposed by Taylor [1]. The asymptotic solution for small amplitudes considers an infinitely long cylindrical (radius r_c) flagellum actuated with waves of sinusoidal lateral displacements of wavelength λ, wave number $k = 2\pi/\lambda$, and amplitude A. Taylor expressed the ratio of the swimming speed (V) to the wavespeed ($U_w = 2\pi f/k$) as

$$\frac{V}{U_w} = \frac{1}{2}A^2k^2\left\{\frac{K_0(z_1) - 1/2}{K_0(z_1) + 1/2}\right\},$$

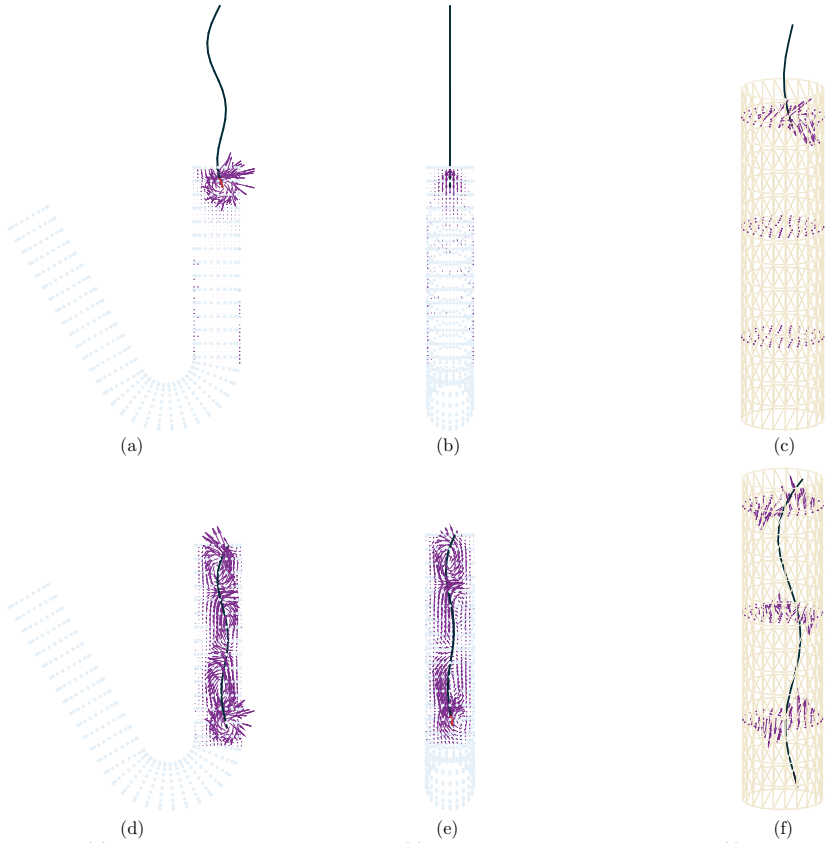

FIG. 4. Flagellum-tube system depicting fluid velocity vectors at representative planes [(a), (d) frontal; (b), (e) sagittal; (c), (f) zoomed-in perspective view of transverse planes] at the time when the swimmer is entering the tube (top row), and later the swimmer is completely inside the tube. Although our model swimmers are completely isotropic, the direction of the wave of preferred curvature is specified, and the filament will swim in the opposite direction. In each of the six panels, the direction of swimming is downward. The front-end (head) of the swimmer is highlighted in red throughout this paper. Here, the flagellum has a length of 50 μm and carries one and one-half sinusoidal waves of amplitude 2 μm. It is discretized with 20 Stokeslet segments, and the regularization parameter, $\epsilon = 1.0$ mm. The tube of radius 6 μm was spatially discretized by circular rings 3.85 mm apart in the axial direction with points on the perimeter of the circles that are separated by 1.8 mm in the azimuthal direction, and the regularization for the Stokeslet surfaces is $\varsigma = 0.1$ nm. We used a time step of 10^{-6} s for all the cases reported.

where $z_1 = kr_c$ (product of wave number and cylinder radius) and K_n is the modified Bessel function of the second kind of order n. Note that in our model, we consider the regularization parameter ϵ as a proxy for flagellar radius.

The differences between our model and the asymptotic approach include (i) finite length, (ii) a finite bending rigidity, and (iii) representation of the cylinder diameter. While the Taylor flagellum is infinitely long, we will compare the asymptotic swimming speeds to those computed for finite-length swimmers of varying length. Also, the theoretical model assumes prescribed kinematics. We instead chose the bending rigidity of the flagellum to be on the order of 10^{-21} J m based on measurements reported in the literature for flagellated swimming micro-organisms [59,60]. This value is large enough so that the achieved amplitude in our preferred curvature model closely matches the prescribed amplitude chosen in the asymptotic calculation.

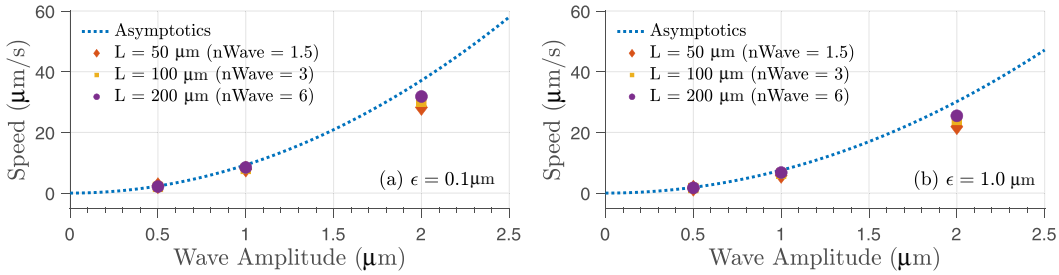

FIG. 5. Comparison of numerical results for a swimming flagellum of finite length to asymptotic expansion for an infinitely long cylinder with planar bending waves. The Stokeslet segment regularization parameter is $\epsilon = 0.1\,\mu$m in (a) and $\epsilon = 1.0\,\mu$m in (b). The segment size for all the cases considered is 2.5 μm.

The continuous curves in Figs. 5(a) and 5(b) show the swimming speed of Taylor's infinite cylindrical flagellum as a function of amplitude for $\lambda = 33.33\,\mu$m, beat frequency $f = 20$ Hz, with $r_c = \epsilon = 0.1\,\mu$m [panel (a)] and $r_c = \epsilon = 1.0\,\mu$m [panel (b)]. We note that the curves in each panel are different because Taylor's solution is a function of flagellar radius r_c. We see that the thicker flagellum swims more slowly than the thinner one, but even when increasing the radius tenfold, the speed only decreases by about 18% (at $A = 2.0\,\mu$m). The symbols show the computed swimming speed for three different values of flagellar length ($L = 50$, 100, and 200 μm). Increasing flagellar length for each amplitude moves the swimming speed closer to the theoretical value, which is evident with the data points for wave amplitude $A = 2.0\,\mu$m. Moreover, the agreement with the asymptotic solution also decreases with increasing amplitude, as expected. Both panels of Fig. 5 show similar agreement between computed velocities and asymptotic velocities. Based on this agreement, we chose the regularization parameter $\epsilon = 1.0\,\mu$m in subsequent simulations. Although this is larger than a typical eukaryotic flagellar radius, this larger regularization parameter allows a larger time step in the computations.

2. Effects of swimmer length and activation on swimming performance

The classical analysis of Taylor that computes a finite swimming velocity for an infinitely long flagellum demonstrates that increasing the length of a flagellum by adding more and more wavelengths of the same amplitude and beat frequency will not continually result in higher swimming velocities. How then does flagellar length affect swimming performance in actual swimmers? Conflicting findings exist in the literature, sometimes correlating them positively [66,67] and sometimes in a totally opposite manner [68–70]. In a study of published experimental data on 141 animal species, Soulsbury *et al.* performed a principal component analysis (PCA) for examining structural clustering of sperm morphology and then compared the model predictions across all morphologically similar sperm clusters [71]. Four out of five clusters in the data set indicated no significant effect of variation of length on swimming speed. Of course, from a fluid dynamics perspective, swimming speed depends upon many factors in addition to flagellar length, including organism morphology and flagellar wave kinematics.

In the case considered here of a planar, filiform flagellum, we take a closer look at the effects of flagellar length on speed, power, and efficiency. In the simulations, speed is tracked on each Stokeslet segment and averaged over a beat period for the values reported. Since the Kirchhoff rod model can independently actuate in the linear and angular motions, the instantaneous power consumption is measured as a sum of linear and angular power as $P_{\text{swim}} = \int_0^L (\mathbf{f}_l \cdot \mathbf{u} + \mathbf{n}_l \cdot \mathbf{w})\,\mathrm{d}s$. We follow Lighthill's definition of Froude efficiency [72] given as

$$\eta = \frac{P_{\text{drag}}}{P_{\text{swim}}} = \frac{\xi_{\parallel} L v_{\text{mean}}^2}{P_{\text{swim}}},$$

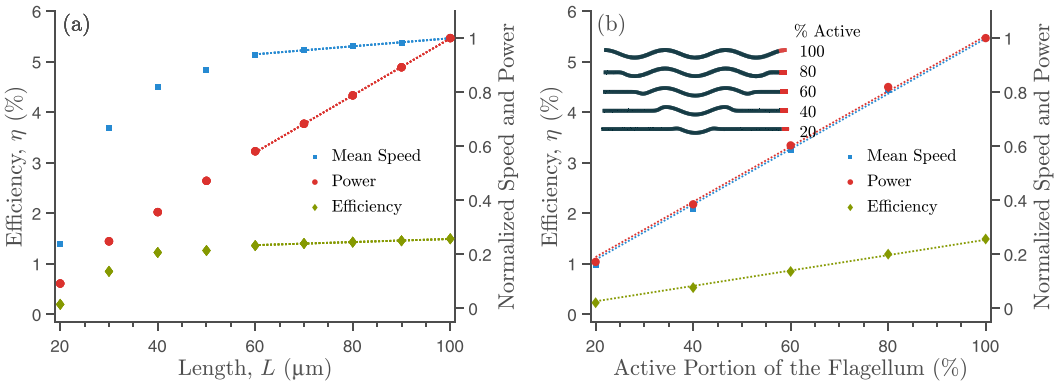

FIG. 6. Free-space swimming performance: Effects of (a) flagellar length and (b) change in active beating portion on swimming speed, power, and efficiency. The swimming speed and power in each panel are normalized with respect to those of the 100 μm flagellum that is active along its entire length (dimensional swimming speed: 33.6 μm/s, power expenditure: 26.6 fw). Bending rigidity, beat frequency, and target shape amplitude are fixed, respectively, at 4.95×10^{-21} J m, 20 Hz, and 2 μm, respectively, for all the cases presented.

4

where $\xi_{\parallel} = \frac{2\pi\mu}{\log(0.18\lambda/\epsilon)}$ is the parallel resistance coefficient [73], and v_{mean} is the mean swimming speed of the flagellum. Starting with a 100 μm long flagellum with three full waves [a wave number of 0.188 μm^{-1}, top image of the inset in Fig. 6(b)], we examine the swimming performance of the flagellum as we shorten its length while keeping the wave number and other kinematics fixed. Figure 6(a) shows the swimming speed, power expenditure, and efficiency computed as a function of flagellar length. The average speed of the flagellum remains fairly constant as the length is reduced until the flagellar length falls below two wavelengths. For even shorter flagella, the speed decreases, with a pronounced drop when it supports less than one wavelength. Calculated power increases linearly with length, while the swimming efficiency is basically constant for flagella that support more than two wavelengths.

Experimental studies with particularly long sperm flagella have reported that along the flagellum, there are sections that are actively beating, interspersed with inactive sections [74]. We examine the hydrodynamic performance of a model flagellum of fixed length, where only a segment of the flagellum is active [Fig. 6(b)]. Here we reduce the active beating portion of the flagellum by setting the preferred curvatures near the head and tail to zero. This results in an "active" middle section with passive ends on both sides. We see that speed, power, and efficiency increase linearly with active portion percentage. For species with very long flagella, such "energy saver" passive states may have evolved to conserve energy for later stages of the fertilization process.

We can also ask, then, what is the cost for a swimmer to carry around inactive sections along its length? To investigate this, we may directly compare the values of speed, power, and efficiency in Figs. 6(a) and 6(b), where the normalization for speed and power in each figure is with respect to the 100 μm flagellum that is active along its entire length. For instance, the values corresponding to the flagellum of length 60 μm in Fig. 6(a) should be compared to the values shown for 60% active portion of the 100 μm flagellum in Fig. 6(b). We see that carrying around the inactive portion at the front and back of the flagellum here gives a swimming speed that is about 60% of the flagellum unencumbered by inactive segments, requires about the same power, but is about 38% less efficient. Even for the cases where the flagellum are so short that they cannot accommodate two full wavelengths [e.g., less than 60 μm long cases in Fig. 6(a)], their swimming speeds remain higher compared to corresponding 100 μm long cases with inactive sections in Fig. 6(b).

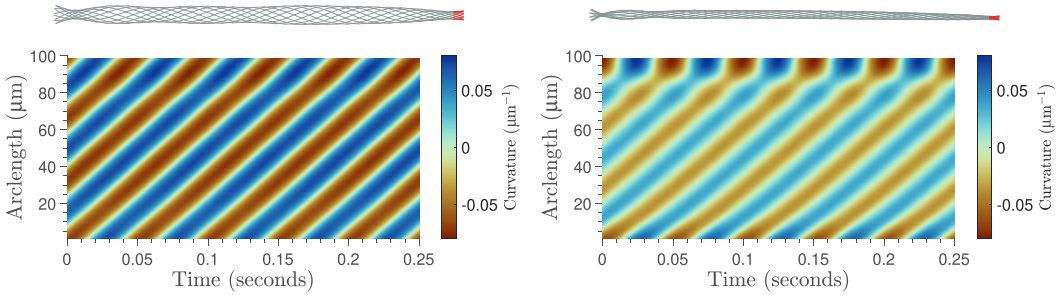

FIG. 7. Influence of the bending stiffness on flagellum actuation dynamics and achieved shapes. In both cases, the flagellum has a length of 100 μm, a preferred amplitude of 2 μm, and a beat frequency of 20 Hz. Flagellar envelope corresponding to each stiffness is shown above. (a) $EI = 4.95 \times 10^{-21}$ J m and (b) $EI = 2.475 \times 10^{-22}$ J m.

3. *Effects of bending stiffness, beat frequency, and the sperm number*

In this preferred curvature model, the flagellum is in pursuit of a traveling wave of a chosen amplitude. The extent to which the preferred kinematics are met depends upon the bending rigidity of the flagellum, in addition to the fluid environment and nearby boundaries. Figure 7(a) shows the envelope of shapes achieved by the long, flexible flagellum and the kymograph of achieved curvature for the model swimmer in free space used as our base case in the previous section ($EI = 4.95 \times 10^{-21}$ J m). These should be compared to Fig. 7(b), whichshows the same for a softer flagellum ($EI = 2.475 \times 10^{-22}$ J m). We see that while both are actuated with the same frequency of 20 Hz, and each figure shows a traveling wave of curvature over five beat periods from head to tail, the emergent amplitude and curvatures along the softer flagellum are greatly diminished.

While eukaryotic flagellar bending rigidity can vary as much as four orders of magnitude between species [59], beat frequencies vary within one to two orders of magnitude [61]. Figure 7 demonstrates that the achieved amplitude of the flagellum is strongly coupled to its bending rigidity. We next examine how emergent shape dynamics are influenced by the frequency of actuation. For instance, for high beat frequencies, the short timescale of actuation could be much smaller than the timescale of elastic relaxation, not allowing the flagellum to come close to the preferred amplitude. We explored these relationships by varying both beat frequency and bending stiffness of the model flagellum over experimentally reported ranges while keeping the geometric parameters of the flagellum fixed. Specifically, for a preferred amplitude of 2 μm, we track the achieved amplitude, swimming speed, required power, and efficiency as a function of beat frequency (varied from 5 to 50 Hz) and bending stiffness (varied from 4.95×10^{-23} J m to 4.95×10^{-20} J m). Figure 8(a) shows a color plot of the achieved amplitude of the flagellum for different beat frequencies and bending rigidities. We see that the preferred amplitude is met for the stiffest flagella at all frequencies, but for midrange stiff flagella, the amplitude is met only for slow actuation. The softest flagella cannot meet the preferred amplitude, and, at high frequencies, barely support a wave. We remark that for flagella with *prescribed* kinematics, swimming speed increases linearly with beat frequency. Here, however, the kinematics are not prescribed, and as beat frequency increases for a fixed bending rigidity, the achieved amplitude decreases, which has a pronounced effect on swimming speed and power.

The swimming speeds and power expenditures are shown in Figs. 8(c) and 8(d). We see that the fastest swimmers and those that require the most power are the stiffest ones, actuated with the highest beat frequencies. Figure 8(b) shows the resulting hydrodynamic efficiency. The most inefficient swimmers are soft flagella driven at high beat frequencies. Using this definition of efficiency, it appears that it would be preferable to be a stiff flagellum with a very small beat

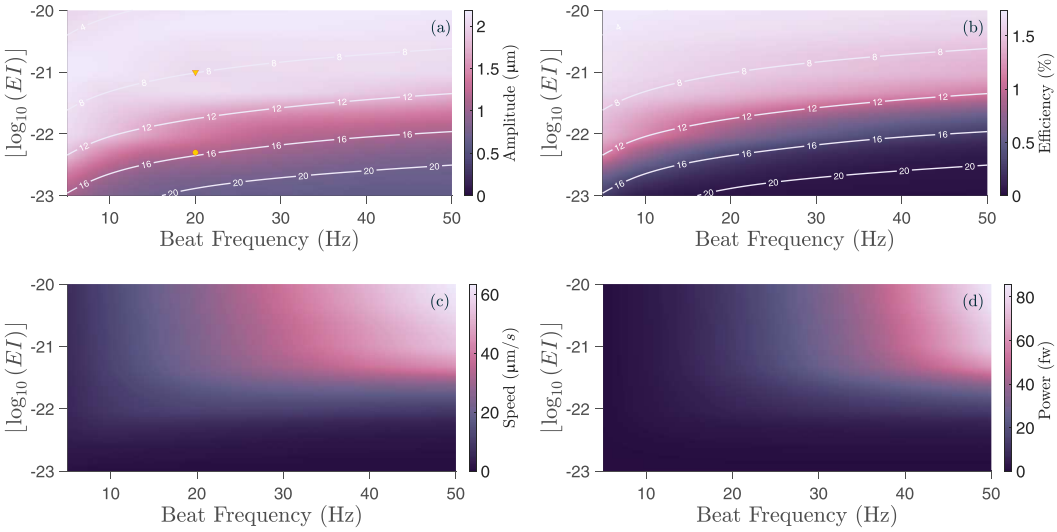

FIG. 8. Effect of beat frequency and bending rigidity on the swimming performance: (a) achieved amplitude, (b) efficiency, (c) speed, and (d) power, in free space. The flagellum length and wave number are fixed at 100 μm and 0.188 μm^{-1}, respectively. The parameter space of bending rigidity and frequency is chosen from experimental measurements reported in the literature [59,61]. The yellow triangle and circle markers on panel (a) represent the locations for the kymographs shown in Figs. 7(a), and 7(b) in the EI vs frequency space, respectively.

frequency [upper left-hand corner of Fig. 8(b)]. Of course, the resulting swimming speed would be very small [upper left-hand corner of Fig. 8(c)], and this flagellar swimmer may never get wherever it needs to go. This certainly demonstrates that this hydrodynamic definition is only one measure of efficiency relevant to a living organism. In a recent related Kirchhoff rod model of gait modulation of undulatory microswimmers, other measures of efficiency that take into account the cost of transport and basal metabolic rate were investigated [75].

As in other models of flexible filaments in a viscous fluid (e.g., [76–80]), we make use of a dimensionless number known as the elastoviscous number or sperm number, Sp, which measures the relative strength of viscous forces to elastic forces:

$$\mathrm{Sp} = \left(\frac{\xi_\perp \omega L^4}{EI}\right)^{1/4}.$$

Here $\xi_\perp$ is the perpendicular resistance coefficient from resistive force theory defined here based on Lighthill's slender body theory [73]. In many cases, the dynamics of the filament-fluid system is determined by the value of this elastoviscous number. For instance, in the case of a passive filament in shear flow, whether it undergoes rigid rotations or S-buckling or snaking motion is determined by the elastoviscous number [77]. Is the hydrodynamic performance of the current flagellar-fluid system determined by Sp alone? In Figs. 8(a), and 8(b), we plot curves of iso-sperm number in the beat frequency versus bending rigidity plane. We see that the values of achieved amplitude and efficiency are determined by this single, nondimensional parameter. However, this is not the case for either swimming speed or power—two flagella with the same preferred amplitude and wavelength, swimming in the same fluid, but with different EI actuated at different frequencies, can have the same Sp but swim at very different speeds. However, their efficiencies could still be the same.

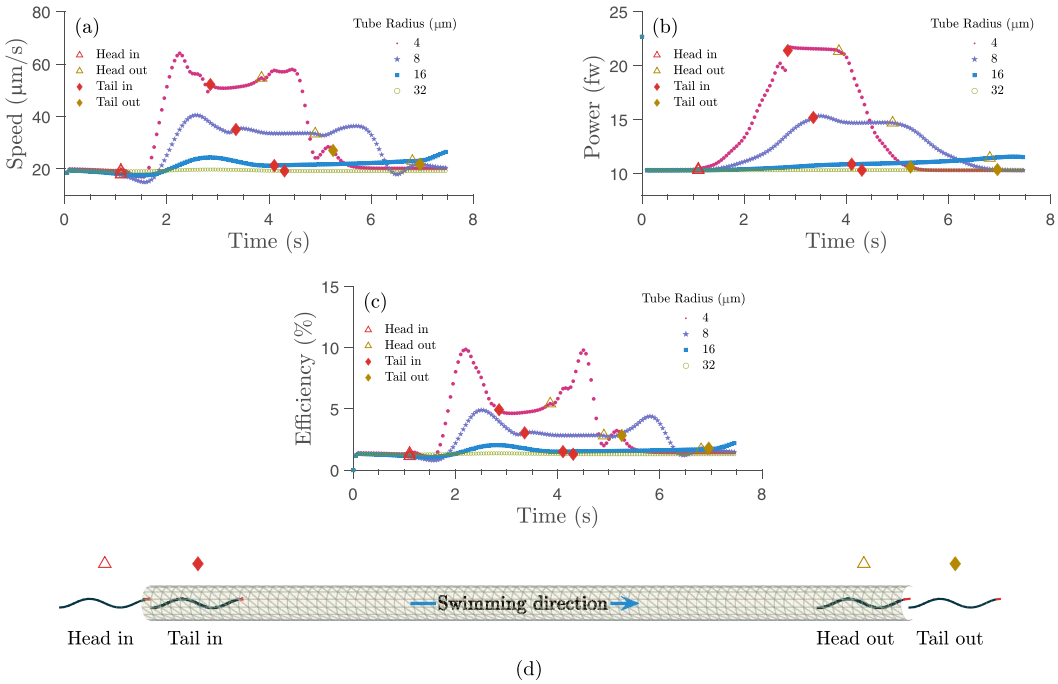

FIG. 9. Swimmer interaction with tubular confinement: (a) speed, (b) power, and (c) efficiency variation as the flagellum enters, swims through, and exits the rigid tubular confinement. Tube length is 400 μm while the fixed flagellar parameters are $L = 50\,\mu\text{m}$, $k = 0.188\,\mu\text{m}^{-1}$, $A = 2\,\mu\text{m}$, $f = 20\,\text{Hz}$, and $EI = 4.95 \times 10^{-21}\,\text{J m}$. (d) Schematic of the position of the swimmer with respect to the tube corresponding to the legend positions (head in, tail in, head out, and tail out).

B. Swimming performance inside tubes

Previous investigations of micro-organism swimming in tubular confinements using minimal models of organisms [81–83] have demonstrated that confinement can give rise to enhanced swimming speed. A model with fully resolved flagella was presented in [84], where an infinitely long, helical flagellum with prescribed kinematics was axially aligned in an infinitely long tube. Here, it was found that the speed of the rotating helix increased as the radius of the tube decreased. More recently, LaGrone *et al.* [44] used a regularized Stokeslet framework to analyze the swimming of finite-length, flexible helices in a cylinder and reported speed enhancement with confinement. We remark that the helical swimmer in [44] was modeled using a surface discretization of the helix, and not using a Kirchhoff rod representation as in the work discussed here.

While the previous sections discussed the hydrodynamic performance of the flexible flagellum in free space, we now examine its performance as it enters, swims through, and exits a straight, finite tube, open at both ends. We analyze the progression of a swimmer that supports one and one-half wavelengths ($L = 50\,\mu\text{m}$), preferred amplitude of $A = 2\,\mu\text{m}$, and with the stiffest bending rigidity used in this work ($EI = 4.95 \times 10^{-21}\,\text{J m}$) through tubes of varying radii. Figure 9 shows the (a) swimming velocity, (b) power expenditure, and (c) efficiency as a function of time for four different radii of the tube ($R = 4,\ 8,\ 16,$ and $32\,\mu\text{m}$). Figure 9(d) shows the schematic of a model swimmer moving through the tube, along with the symbols used to designate the times when the head enters, when the tail is fully in the tube, when the head leaves the tube, and then when the tail is finally out of the tube. All swimmers were initialized in a plane that contained the tube axis. First, we remark that the speed, power, and efficiency for the swimmer in a tube of radius $R = 32\,\mu\text{m}$ are indistinguishable from the free-space values. Figure 9(a) shows that for $R = 4,\ 8,$ and $16\,\mu\text{m}$, there

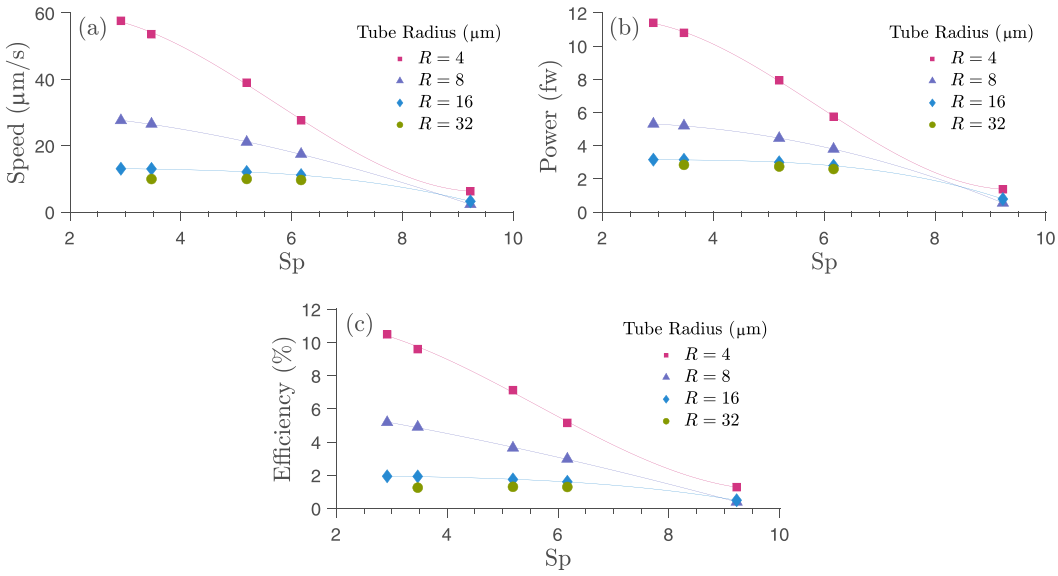

FIG. 10. Effects of sperm number (Sp) on swimming performance (a) speed, (b) power, and (c) efficiency in different tube radii. Bending rigidity, and hence Sp, was varied, but all other flagellar parameters were as in Fig. 9. The data fit used a cubic polynomial.

is a dip from free-space velocity as the head nears the tube entrance. However, this is followed by a rapid boost in swimming speed, which reaches its maximum when the flagellum is partially within the tube. This boost increases as the radius of the tube decreases. As the flagellum starts to swim out from the tube, we surprisingly find yet another boost in speed. As with the speed profiles, power requirements, and swimming efficiency are also elevated inside the confinement. These results are consistent with results in [44,84]. While inside the tube, the power requirements are significantly higher than in free space, and they increase with the level of confinement [Fig. 9(b)]. Since the length is fixed in all cases, the efficiency here is proportional to the ratio of the square of the swimming speed over the power, reflecting a similar pattern to the swimming speed plot [Fig. 9(c)]. Compared to its performance in free space, when in a tube whose radius is four times its preferred amplitude, a 120% rise in power requirement is accompanied by about a 200% boost in speed, which results in a net positive increase in swimming efficiency inside the confinement.

The resulting swimming motion of the flagellum through the enclosure is a result of forces due to Kirchhoff rod actuation, boundary forces on the surface elements, as well as the repulsion forces in Eq. (16). Because the Stokes equations are linear, we can isolate the contribution of each of these three forces to the velocity of any point on the flagellum. In the simulation in Fig. 11(a) with $R =$ 8 μm below, the repulsion contribution to the instantaneous speed of the midpoint of the flagellum is 8–10 orders of magnitude smaller than contributions from the other forces as the swimmer traverses the tube. We are, therefore, confident that this repulsion does not alter the overall dynamics of the system.

We now consider the hydrodynamic performance of swimmers of different bending rigidities (hence different sperm numbers Sp), when their full lengths are within tubes of different radii. Figure 10(a) shows the swimming speed as a function of Sp for swimmers in all four confinements. For the stiffest flagellum (Sp = 2.91), when the tube radius is halved, the swimming speed doubles. For softer swimmers (higher Sp), flagella receive a speed boost with confinement, but the difference diminishes as Sp increases. Although this Kirchhoff rod formulation can model extensible filaments, here we choose the shear and stretch moduli (b_1, b_2, b_3) large enough so that the rod remains inextensible to within a few percent. With these choices, the arclength parametrization is valid. The

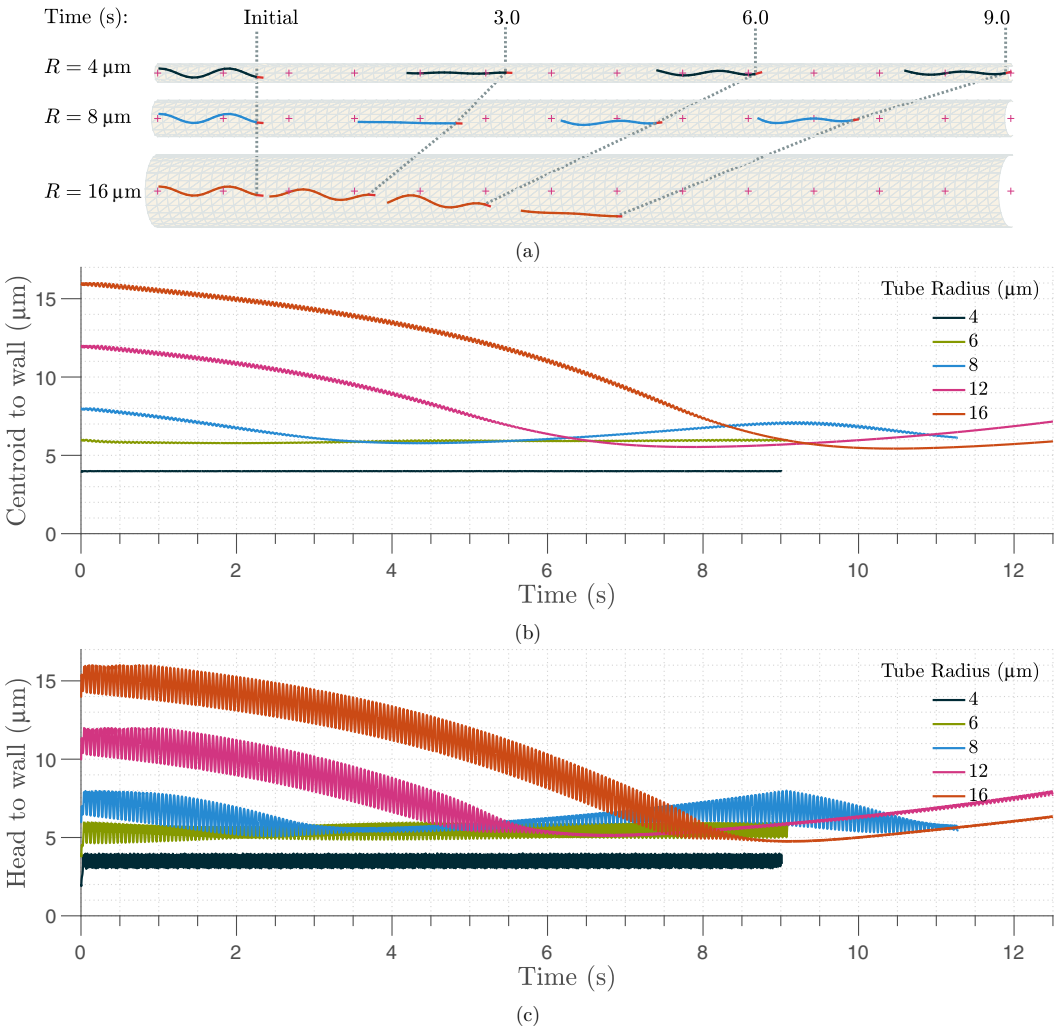

FIG. 11. Drift of the flagellum toward the tube walls. Top panel shows some representative setup where a 50-µm-long flagellum with a preferred beat amplitude of 2 µm swims through tubes of different radii ranging from 4 to 16 µm. The middle panel tracks the swimmer's geometric centroid to wall distance, while the bottom panel shows the oscillating head distance from the wall for the same swimmers.

power and efficiency follow similar trends [Figs. 10(b) and 10(c)]. We also note that for a given tube radius, as the flagellar stiffness is lowered (increasing Sp), we observe a steady drop in speed, power, and efficiencies. Beyond Sp = 8.5, the flagellum is too floppy to achieve an amplitude to swim inside the confinement, hence the speed boost for tighter confinements at Sp = 8.5 is negligible.

C. Drift toward boundaries and bend navigation

Several experimental works involving microswimmers near boundaries have observed interesting behavior including accumulation near rigid boundaries, circular trajectories of swimming after accumulation, and rheotaxis in background flow [18,85–87]. Theoretical models using the method of images with slender body theory, regularized Stokeslets, and immersed boundary approaches have reproduced such behavior and offered mechanistic explanations for both planar and helical

swimmers near a flat boundary [12,37,40,88,89]. Most biological microswimmers have to traverse narrow, confined, and tortuous fluid-filled passages. For example, a common fruitfly (*Drosophila*) sperm inside the female reproductive tract are stored in coiled sperm storage receptacles. The swimmers must adapt their swimming trajectories to move through the surrounding confinements. Additionally, experiments with mammalian sperm cells found direct effects of bounding curved surface on changes in swimming mode [13] as well as boundary following behaviors [90]. Using regularized Stokeslet surfaces, we extend the framework to simulate such tracts with biologically relevant geometrical features (e.g., nonuniform radii, wide or narrow bends, etc.) that can predict the shape deformations and trajectories of the flagellum as it moves through the tubular structure.

Here we examine more closely a flagellum with a preferred planar beat moving in straight tubes of varying radii (Fig. 11). Several features of swimming behavior are observed. First, as highlighted previously, narrowing confinements significantly boost swimming speed, as can be seen in Fig. 11(a). Interestingly, while the flagella are initialized centered on the tube axis, in larger tubes, we see a drift toward the tube surface. We can quantify this drift by examining the time evolution of the distance of the centroid of the swimmer to the nearest position on the tube wall [Fig. 11(b)]. Tubes with small diameters show little drift (e.g., black line for the 4-μm-tube case). Figure 11(c) tracks the bobbing motion of the "head" of the swimmer. Even though the swimmers in each tube have the same preferred amplitude, here we can see that the achieved amplitude of the head excursion is diminished in tighter confinements. In the simulations where drift is apparent in Fig. 11(c), there is a whole-body twist marked by the flattening of the up-down oscillation (for instance, around the 6-s mark for the pink line of the 12 μm case). This indicates that the beat plane of the flagellum rotates during the simulation.

This intriguing behavior, where tighter confinement leads to straighter swimmer trajectories about the central axis of the confinement, has recently been observed in both laboratory experiments and computational studies. For instance, in tracking swimming paths of *E. coli* in microfabricated channels of different cross sections, Vizsnyicai *et al*. [91] observe, "in large channels, bacteria always crash onto confining walls, when the cross section falls below a threshold, they leave the walls to move swiftly on a stable swimming trajectory along the channel axis." Similarly, experiments by Jana *et al*. [92] found that paramecium swimming paths transition from oscillatory, helical trajectories to straight lines as the diameter of the capillary tube decreased. Experiments with *E. coli* confined between two flat boundaries observed circular motion near the bottom in taller channels (height larger than 3 μm), and trajectories that either oscillated between top and bottom boundaries or straight swimming at the center of the channel for channel heights smaller than 2.5 μm [93]. This same behavior was demonstrated *in silico* by a model of a flexible rotating helix swimming in a tube [44]. That study found that when the helical swimmer's axis was initially not aligned with the tube axis, for small enough tube radii, the swimmer centered itself so that alignment occurred. Another computational model of a helical swimmer between two parallel plates [94] also demonstrated centering trajectories for small channel heights. Moreover, this centering behavior for spheroidal squirmers inside a tubular enclosure was also reported in [82].

Finally, we describe observations made when using this framework to model the flexible flagellum as it moves through a curved tube. Figure 12 shows the progression of a swimmer as it approaches a 120° bend in the tube. As it moves through bent tubular confinement, the wall interactions cause it to change its oscillatory motion and curvature to navigate the bend of the tube. In fact, because the length of this swimmer is greater than the straight portion of the tube, it must be flexible enough to bend out of its preferred planar shape to make its way through the enclosure. The orientation of the oscillation plane at points of the flagellum that are near the tube surface aligns itself with the tangent plane at that location of the tube. Figures 12(a)–12(d) also highlight (in purple) a patch of the plane where the head of the flagellum oscillates. The wall interactions cause the flagellum to twist and change its beat-plane orientation to result in a slithering motion along the tube wall. The wall interactions also affect the rest of the flagellum, even the portions that are not

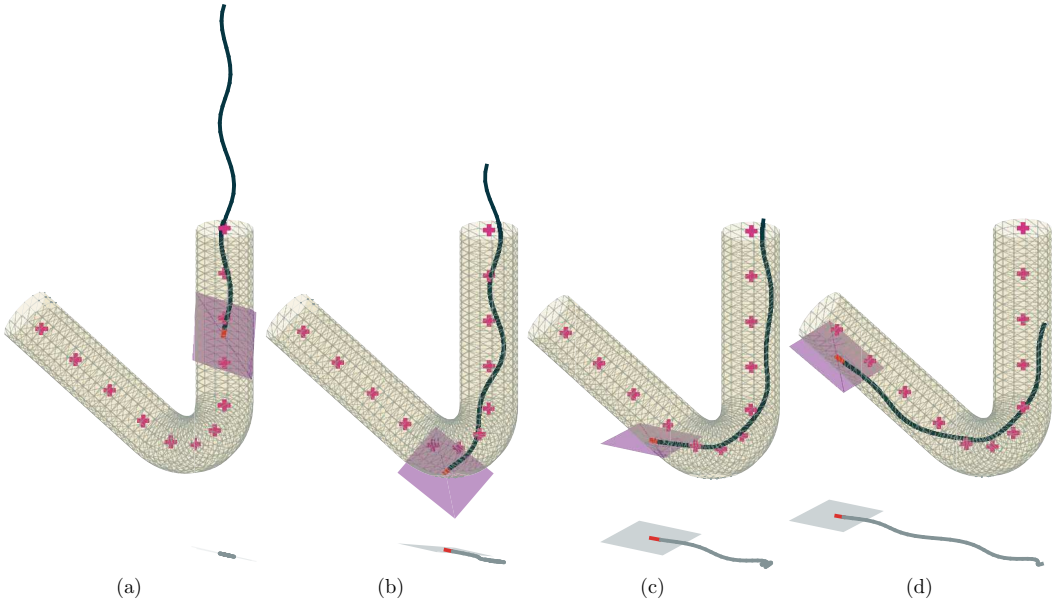

FIG. 12. Flagellum navigating a 120° bend (left-to-right) of a tubular enclosure. The flagellum beats in a planar sinusoidal shape in free space. The beat plane at the head section is highlighted in purple, and the initial head section (first Stokeslet segment) is red. Also depicted is the projected view of the flagellum from above. The tube length is 150 μm and its diameter is 16 μm. The flagellar parameters are $L = 100\,\mu\text{m}$, $k = 0.188\,\mu\text{m}^{-1}$, $A = 2\,\mu\text{m}$, $f = 20\,\text{Hz}$, and $EI = 4.95 \times 10^{-21}\,\text{J m}$.

in proximity to the wall. In particular, the swimmer goes through a slight buckling, resulting in an out-of-plane bend that allows it to traverse the curved tube.

IV. CONCLUSION

Inspired by long flagellated filiform swimmers that must navigate extremely narrow bends in nature [23,95], here we model a flexible, flagellar swimmer moving through both straight and bent tubular confinements. Our focus in this paper is to outline how recent improvements to the regularized Stokeslet framework can be leveraged to describe the coupled system. We use Kirchhoff rod theory with regularized Stokeslet segments to model the flagellum efficiently by requiring only the discretization of the flagellum centerline [45] and using analytical formulas for the fluid velocity due to linearized forces along each segment. This allows us to represent the flagellum with a relatively small number of segments. The confinement provided by the tubes is modeled with regularized Stokeslet surfaces [47]. Analogous to the segments, this method requires relatively few surface patches with linearized forces.

This model does not prescribe flagellar kinematics; rather, the flexible flagellum is in pursuit of a preferred, time-dependent curvature, and its shape emerges from the coupling with the viscous fluid and the confinement. Here, for simplicity, we choose a preferred curvature corresponding to a single-mode flagellar waveform. Models of flagellar beating that predict flagellar shapes due to internally generated stresses, however, can generate more complex waveforms (e.g., [96]). The computational framework presented here can readily be extended to include these preferred shapes.

We first explored the hydrodynamic performance of flexible swimmers in free space. We found that the inclusion of inactive flagellar regions causes the flagellum to swim more slowly than the corresponding shorter flagellum that is active along its entire length. However, there is little change in power expenditure when inactive sections are present. We also explored how beat frequency

and bending rigidity of these actuated flagella affected the achieved amplitude and hydrodynamic performance. While we found that the achieved amplitude was a function of the nondimensional sperm number (Sp), the speed and power expenditure were not. For example, while a very flexible flagellum actuated with a small beat frequency could operate at the same Sp as a stiff flagellum actuated with a large beat frequency, the stiff swimmer expends more power and swims faster than the softer swimmer. We do find, however, that the efficiency is, indeed, a function of Sp.

For flagella moving into and out of straight tubular confinements, we found a significant boost in swimming speed as the confinement narrowed, with this boost declining for floppier flagella. Our model also demonstrates a clear drift of the flagellum, initialized about the axis of a tube, toward the tube surface when the tube radius exceeds a threshold value (how this value depends upon flagellar material properties, length, and wave kinematics remains to be quantified). As the model swimmers drive towards the tube wall, they exhibit slithering along the surface, a behavior discovered for mammalian sperm [13]. In the simulation presented with the curved tube, the anterior part of the flagellum slithers near the surface, while the rest of the flagellum beats in a different plane. In future work, we will investigate the interplay of tube geometry, flagellar material properties, preferred-curvature parameters, and fluid properties on the ability of these filiform swimmers to navigate curved passages and their corresponding hydrodynamic performance.

ACKNOWLEDGMENTS

FQ This research was supported by the Human Frontiers of Science Program Grant No. RGP0017/2022 [97], the National Science Foundation Grant No. DMS 2054333, and the Simons Foundation Grant No. SFI- MPS-SFM-00006482. We gratefully acknowledge the many stimulating discussions with our HFSP group: Rhonda Snook, Stuart Humphries, Carl Soulsbury, Kamil Talar, Jessica Frith, Jessica Hadlow, and Erin Macartney.

DATA AVAILABILITY

10 The data that support the findings of this article are openly available [?].

[1] G. I. Taylor, The action of waving cylindrical tails in propelling microscopic organisms, Proc. R. Soc. London A **211**, 225 (1952).
[2] M. Sauzade, G. J. Elfring, and E. Lauga, Taylor's swimming sheet: Analysis and improvement of the perturbation series, Physica D **240**, 1567 (2011).
[3] L. J. Fauci and R. Dillon, Biofluidmechanics of reproduction, Annu. Rev. Fluid Mech. **38**, 371 (2006).
[4] J. S. Guasto, R. Rusconi, and R. Stocker, Fluid mechanics of planktonic microorganisms, Annu. Rev. Fluid Mech. **44**, 373 (2012).
[5] E. Lauga and T. R. Powers, The hydrodynamics of swimming microorganisms, Phys. Rev. Fluids **72**, 096601 (2009).
[6] E. Lauga, Bacterial hydrodynamics, Annu. Rev. Fluid Mech. **48**, 105 (2016).
[7] L. Zhang, J. J. Abbott, L. Dong, K. E. Peyer, B. E. Kratochvil, H. Zhang, C. Bergeles, and B. J. Nelson, Characterizing the swimming properties of artificial bacterial flagella, Nano Lett. **9**, 3663 (2009).
[8] E. Gaffney, H. Gadêlha, D. Smith, J. Blake, and J. Kirkman-Brown, Mammalian sperm motility: Observation and theory, Annu. Rev. Fluid Mech. **43**, 501 (2011).
[9] M. Köttgen, A. Hofherr, W. Li, K. Chu, S. Cook, C. Montell, and T. Watnick, Drosophila sperm swim backwards in the female reproductive tract and are activated via TRPP2 Ion channels, PLoS ONE **6**, e20031 (2011).

[10] L. Le Nagard, A. T. Brown, A. Dawson, V. A. Martinez, W. C. K. Poon, and M. Staykova, Encapsulated bacteria deform lipid vesicles into flagellated swimmers, Proc. Natl. Acad. Sci. USA **119**, e2206096119 (2022).
[11] T. Bhattacharjee and S. S. Datta, Bacterial hopping and trapping in porous media, Nat. Commun. **10**, 2075 (2019).
[12] D. Kim, Y. Kim, and S. Lim, Effects of swimming environment on bacterial motility, Phys. Fluids **34**, 031907 (2022).
[13] R. Nosrati, A. Driouchi, C. M. Yip, and D. Sinton, Two-dimensional slither swimming of sperm within a micrometre of a surface, Nat. Commun. **6**, 8703 (2015).
[14] D. Smith, E. Gaffney, H. Shum, H. Gadêlha, and J. Kirkman-Brown, Comment on the article by J. Elgeti, U. B. Kaupp, and G. Gompper: Hydrodynamics of sperm cells near surfaces, Biophys. J. **100**, 2318 (2011).
[15] J. Elgeti, U. B. Kaupp, and G. Gompper, Response to comment on article: Hydrodynamics of sperm cells near surfaces, Biophys. J. **100**, 2321 (2011).
[16] M. T. Bryan, J. Garcia-Torres, E. L. Martin, J. K. Hamilton, C. Calero, P. G. Petrov, C. P. Winlove, I. Pagonabarraga, P. Tierno, F. Sagués, and F. Y. Ogrin, Microscale magneto-elastic composite swimmers at the air-water and water-solid interfaces under a uniaxial field, Phys. Rev. Appl. **11**, 044019 (2019).
[17] M. Morse, A. Huang, G. Li, M. R. Maxey, and J. X. Tang, Molecular adsorption steers bacterial swimming at the air/water interface, Biophys. J. **105**, 21 (2013).
[18] V. Rothschild, Non-random distribution of bull spermatozoa in a drop of sperm suspension, Nature (London) **198**, 1221 (1963).
[19] A. P. Berke, L. Turner, H. C. Berg, and E. Lauga, Hydrodynamic attraction of swimming microorganisms by surfaces, Phys. Rev. Lett. **101**, 038102 (2008).
[20] S. Suarez and A. A. Pacey, Sperm transport in the female reproductive tract, Hum. Reprod. Update. **12**, 23 (2006).
[21] M. Zaferani, S. S. Suarez, and A. Abbaspourrad, Mammalian sperm hyperactivation regulates navigation via physical boundaries and promotes pseudo-chemotaxis, Proc. Natl. Acad. Sci. USA **118**, e2107500118 (2021).
[22] Denissenko, V. Kantsler, D. J. Smith, and J. Kirkman-Brown, Human spermatozoa migration in microchannels reveals boundary-following navigation, Proc. Natl. Acad. Sci. USA **109**, 8007 (2012).
[23] Y. Yang and X. Lu, Drosophila sperm motility in the reproductive tract, Biol. Reprod. **84**, 1005 (2011).
[24] M. Curtis, J. Kirkman-Brown, T. Connolly, and E. Gaffney, Modelling a tethered mammalian sperm cell undergoing hyperactivation, J. Theor. Biol. **309**, 1 (2012).
[25] J. J. L. Higdon, The hydrodynamics of flagellar propulsion: Helical waves, J. Fluid Mech. **94**, 331 (1979).
[26] N. Ho, S. D. Olson, and K. Leiderman, Swimming speeds of filaments in viscous fluids with resistance, Phys. Rev. E **93**, 043108 (2016).
[27] O. S. Pak, S. E. Spagnolie, and E. Lauga, Hydrodynamics of the double-wave structure of insect spermatozoa flagella, J. R. Soc. Interface. **9**, 1908 (2012).
[28] L. J. Fauci and C. S. Peskin, A computational model of aquatic animal locomotion, J. Comput. Phys. **77**, 85 (1988).
[29] K. Ishimoto and E. A. Gaffney, An elastohydrodynamical simulation study of filament and spermatozoan swimming driven by internal couples, IMA J. Appl. Math. **83**, 655 (2018).
[30] J. Simons, L. Fauci, and R. Cortez, A fully three-dimensional model of the interaction of driven elastic filaments in a stokes flow with applications to sperm motility, J. Biomech. **48**, 1639 (2015).
[31] B. Thomases and R. D. Guy, The role of body flexibility in stroke enhancements for finite-length undulatory swimmers in viscoelastic fluids, J. Fluid Mech. **825**, 109 (2017).
[32] S. D. Olson, S. S. Suarez, and L. J. Fauci, Coupling biochemistry and hydrodynamics captures hyperactivated sperm motility in a simple flagellar model, J. Theor. Biol. **283**, 203 (2011).
[33] B. Chakrabarti and D. Saintillan, Spontaneous oscillations, beating patterns, and hydrodynamics of active microfilaments, Phys. Rev. Fluids **4**, 043102 (2019).

[34] V. F. Geyer, Sartori, F. Jülicher, and J. Howard, Computational modeling of dynein activity and the generation of flagellar beating waveforms, in *Dyneins: Structure, Biology and Disease*, 2nd ed., edited by S. M. King (Elsevier, Amsterdam, 2018), Vol. 2, pp. 192–212.
[35] V. Bayly and S. K. Dutcher, Steady dynein forces induce flutter instability and propagating waves in mathematical models of flagella, J. R. Soc. Interface **13**, 20160523 (2016).
[36] M. Ramia, D. Tullock, and N. Phan-Thien, The role of hydrodynamic interaction in the locomotion of microorganisms, Biophys. J. **65**, 755 (1993).
[37] L. J. Fauci and A. McDonald, Sperm motility in the presence of boundaries, Bltn. Mathcal. Biol. **57**, 679 (1995).
[38] D. J. Smith, E. A. Gaffney, J. R. Blake, and J. C. Kirkman-Brown, Human sperm accumulation near surfaces: A simulation study, J. Fluid Mech. **621**, 289 (2009).
[39] B. U. Felderhof, Swimming and peristaltic pumping between two plane parallel walls, J. Fluid Mech. **21**, 204106 (2009).
[40] S. E. Spagnolie and E. Lauga, Hydrodynamics of self-propulsion near a boundary: Predictions and accuracy of far-field approximations, J. Fluid Mech. **700**, 105 (2012).
[41] A. Bilbao, E. Wajnryb, S. A. Vanapalli, and J. Blawzdziewicz, Nematode locomotion in unconfined and confined fluids, Phys. Fluids **25**, 081902 (2013).
[42] J. Ainley, S. Durkin, R. Embid, Boindala, and R. Cortez, The method of images for regularized stokeslets, J. Comput. Phys. **227**, 4600 (2008).
[43] J. R. Blake, A note on the image system for a stokeslet in a no-slip boundary, Math. Proc. Cambridge Philos. Soc. **70**, 303 (1971).
[44] J. LaGrone, R. Cortez, and L. Fauci, Elastohydrodynamics of swimming helices: Effects of flexibility and confinement, Phys. Rev. Fluids **4**, 033102 (2019).
[45] R. Cortez, Regularized stokeslet segments, J. Comput. Phys. **375**, 783 (2018).
[46] S. D. Olson, S. Lim, and R. Cortez, Modeling the dynamics of an elastic rod with intrinsic curvature and twist using a regularized stokes formulation, J. Comput. Phys. **238**, 169 (2013).
[47] D. Ferranti and R. Cortez, Regularized stokeslet surfaces, J. Comput. Phys. **508**, 113004 (2024).
[48] S. Lim, A. Ferent, X. S. Wang, and C. S. Peskin, Dynamics of a closed rod with twist and bend in fluid, SIAM J. Sci. Comput. **31**, 273 (2008).
[49] D. M. Phillips, Insect sperm: Their structure and morphogenesis, J. Cell Biol. **44**, 243 (1970).
[50] L. Carichino and S. D. Olson, Emergent three-dimensional sperm motility: Coupling calcium dynamics and preferred curvature in a Kirchhoff rod model, Math. Med. Biol. **36**, 439 (2019).
[51] G. J. Hancock, The self-propulsion of microscopic organisms through liquids, Proc. R. Soc. London A **217**, 96 (1953).
[52] G. K. Batchelor, *An Introduction to Fluid Dynamics* (Cambridge University Press, 1967), p. 668.
[53] R. Cortez, The method of regularized stokeslets, SIAM J. Sci. Comput. **23**, 1204 (2001).
[54] M. Gomendio and E. R. S. Roldan, Sperm competition influences sperm size in mammals, Proc. R. Soc. London Ser. B **243**, 181 (1991).
[55] R. Snook, Sperm in competition: Not playing by the numbers, Trends Ecol. Evol. **20**, 46 (2005).
[56] M. Kumar and A. M. Ardekani, Effect of external shear flow on sperm motility, Soft Matter **15**, 6269 (2019).
[57] M. Okuno and Y. Hiramoto, Direct measurements of the stiffness of echinoderm sperm flagella, J. Exp. Biol. **79**, 235 (1979).
[58] G. Xu, K. S. Wilson, R. J. Okamoto, J.-Y. Shao, S. K. Dutcher, and P. V. Bayly, Flexural rigidity and shear stiffness of flagella estimated from induced bends and counterbends, Biophys. J. **110**, 2759 (2016).
[59] S. Ishijima and Y. Hiramoto, Flexural rigidity of echinoderm sperm flagella, Cell Struct. Funct. **19**, 349 (1994).
[60] D. W. Pelle, C. J. Brokaw, K. A. Lesich, and C. B. Lindemann, Mechanical properties of the passive sea urchin sperm flagellum, Cell Motil. Cytoskel. **66**, 721 (2009).
[61] M. Werner and L. W. Simmons, Insect sperm motility, Biol. Rev. **83**, 191 (2008).

[62] K. Ishimoto and E. A. Gaffney, Boundary element methods for particles and microswimmers in a linear viscoelastic fluid, J. Fluid Mech. **831**, 228 (2017).
[63] G.-J. Li and A. M. Ardekani, Hydrodynamic interaction of microswimmers near a wall, Phys. Rev. E **90**, 013010 (2014).
[64] J. F. Brady and G. Bossis, The rheology of concentrated suspensions of spheres in simple shear flow by numerical simulation, J. Fluid Mech. **155**, 105 (1985).
[65] T. Ishikawa and T. J. Pedley, Diffusion of swimming model micro-organisms in a semi-dilute suspension, J. Fluid Mech. **588**, 437 (2007).
[66] M. Tourmente, M. Gomendio, and E. R. Roldan, Sperm competition and the evolution of sperm design in mammals, BMC Evol. Biol. **11**, 12 (2011).
[67] S. Lüpold, S. Calhim, S. Immler, and T. R. Birkhead, Sperm morphology and sperm velocity in passerine birds, Proc. R. Soc. B. **276**, 1175 (2009).
[68] E. R. A. Cramer, E. Garcia-del Rey, L. E. Johannessen, T. Laskemoen, G. Marthinsen, A. Johnsen, and J. T. Lifjeld, Longer sperm swim more slowly in the canary islands chiffchaff, Cells **10**, 1358 (2021).
[69] A. Rojas Mora, M. Meniri, S. Ciprietti, and F. Helfenstein, Is sperm morphology functionally related to sperm swimming ability? A case study in a wild passerine bird with male hierarchies, BMC Evol. Biol. **18**, 142 (2018).
[70] Y. Yang, H. Zhang, S. Wang, W. Yang, J. Ding, and Y. Zhang, Variation in sperm morphology and performance in tree sparrow (*Passer montanus*) under long-term environmental heavy metal pollution, Ecotoxicol. Environ. Saf. **197**, 110622 (2020).
[71] C. D. Soulsbury and S. Humphries, Biophysical determinants and constraints on sperm swimming velocity, Cells **11**, 3360 (2022).
[72] S. Childress, A thermodynamic efficiency for stokesian swimming, J. Fluid Mech. **705**, 77 (2012).
[73] J. Lighthill, Flagellar hydrodynamics, SIAM Rev. **18**, 161 (1976).
[74] R. Rikmenspoel, The equation of motion for sperm flagella, Biophys. J. **23**, 177 (1978).
[75] L. Deutz, Gait modulation of undulatory microswimmers through the lens of optimality, Ph.D. thesis, University of Leeds, 2024.
[76] A.-K. Tornberg and M. J. Shelley, Simulating the dynamics and interactions of flexible fibers in stokes flows, J. Comput. Phys. **196**, 8 (2004).
[77] Y. Liu, B. Chakrabarti, D. Saintillan, A. Lindner, and O. Du Roure, Morphological transitions of elastic filaments in shear flow, Proc. Natl. Acad. Sci. USA **115**, 9438 (2018).
[78] B. Chakrabarti, Y. Liu, J. LaGrone, R. Cortez, L. Fauci, O. Du Roure, D. Saintillan, and A. Lindner, Flexible filaments buckle into helicoidal shapes in strong compressional flows, Nat. Phys. **16**, 689 (2020).
[79] M. T. Gallagher, J. C. Kirkman-Brown, and D. J. Smith, Axonemal regulation by curvature explains sperm flagellar waveform modulation, PNAS Nexus **2**, pgad072 (2023).
[80] E. Lauga, Floppy swimming: Viscous locomotion of actuated elastica, Phys. Rev. E **75**, 041916 (2007).
[81] A. Zöttl and H. Stark, Periodic and quasiperiodic motion of an elongated microswimmer in poiseuille flow, Eur. Phys. J. E **36**, 4 (2013).
[82] L. Zhu, E. Lauga, and L. Brandt, Low-Reynolds-number swimming in a capillary tube, J. Fluid Mech. **726**, 285 (2013).
[83] R. Ledesma-Aguilar and J. M. Yeomans, Enhanced motility of a microswimmer in rigid and elastic confinement, Phys. Rev. Lett. **111**, 138101 (2013).
[84] B. Liu, K. S. Breuer, and T. R. Powers, Propulsion by a helical flagellum in a capillary tube, Phys. Fluids **26**, 011701 (2014).
[85] H. Winet, Wall drag on free-moving ciliated micro-organisms, J. Exp. Biol. **59**, 753 (1973).
[86] D. Woolley, Motility of spermatozoa at surfaces, Reproduction **126**, 259 (2003).
[87] E. Lauga, W. R. DiLuzio, G. M. Whitesides, and H. A. Stone, Swimming in circles: Motion of bacteria near solid boundaries, Biophys. J. **90**, 400 (2006).
[88] K. Ishimoto and E. A. Gaffney, Fluid flow and sperm guidance: A simulation study of hydrodynamic sperm rheotaxis, J. R. Soc. Interface. **12**, 20150172 (2015).
[89] Y. Park, Y. Kim, and S. Lim, Flagellated bacteria swim in circles near a rigid wall, Phys. Rev. E **100**, 063112 (2019).

[90] M. R. Raveshi, M. S. A. Halim, S. N. Agnihotri, M. K. O'Bryan, A. Neild, and R. Nosrati, Curvature in the reproductive tract alters sperm–surface interactions, Nat. Commun. **12**, 3446 (2021).
[91] G. Vizsnyiczai, G. Frangipane, S. Bianchi, F. Saglimbeni, D. Dell'Arciprete, and R. Di Leonardo, A transition to stable one-dimensional swimming enhances *E. Coli* motility through narrow channels, Nat. Commun. **11**, 2340 (2020).
[92] S. Jana, S. H. Um, and S. Jung, Paramecium swimming in capillary tube, Phys. Fluids **24**, 041901 (2012).
[93] J.-M. Swiecicki, O. Sliusarenko, and D. B. Weibel, From swimming to swarming: *Escherichia coli* cell motility in two-dimensions, Integr. Biol. **5**, 1490 (2013).
[94] H. Shum and E. A. Gaffney, Hydrodynamic analysis of flagellated bacteria swimming near one and between two no-slip plane boundaries, Phys. Rev. E **91**, 033012 (2015).
[95] M. K. Manier, J. M. Belote, K. S. Berben, D. Novikov, W. T. Stuart, and S. Pitnick, Resolving mechanisms of competitive fertilization success in drosophila melanogaster, Science **328**, 354 (2010).
[96] S. Camalet, F. Jülicher, and J. Prost, Self-organized beating and swimming of internally driven filaments, Phys. Rev. Lett. **82**, 1590 (1999).
[97] https://doi.org/10.52044/HFSP.RGP00172022.pc.gr.153610.